Focal cortical dysplasia type II-dependent maladaptive myelination in the human frontal lobe

Catharina Donkels[1], Susanne Huber[1], Theo Demerath[2], Christian Scheiwe[3], Mukesch J. Shah[3], Marcel Heers[4], Horst Urbach[2], Andreas Schulze-Bonhage[4,8], Marco Prinz[5,6], Ute Häussler[1,8], Andreas Vlachos[7,8], Jürgen Beck[3], Julia M. Nakagawa[3*], Carola A. Haas[1,8**]

[1]Experimental Epilepsy Research, Department of Neurosurgery, Medical Center - University of Freiburg, Faculty of Medicine, University of Freiburg, Germany

[2]Department of Neuroradiology, Medical Center-University of Freiburg, Faculty of Medicine, 79106 Freiburg, Germany

[3]Department of Neurosurgery, Medical Center - University of Freiburg, Faculty of Medicine, University of Freiburg, Germany

[4]Epilepsy Center Freiburg, Medical Center - University of Freiburg, Faculty of Medicine, University of Freiburg, Germany

[5]Institute of Neuropathology, Medical Center - University of Freiburg, Faculty of Medicine, University of Freiburg, Germany

[6]Signalling Research Centers BIOSS and CIBSS, University of Freiburg, Germany

[7]Department of Neuroanatomy, Institute of Anatomy and Cell Biology, Faculty of Medicine, University of Freiburg, Germany

[8]BrainLinks-BrainTools Center, University of Freiburg, Germany

*Equal contribution

Corresponding author: Dr. Catharina Donkels; email: catharina.donkels@uniklinik-freiburg.de

ORCID IDs: Catharina Donkels: 0000-0003-2636-3873; Theo Demerath: 0000-0002-5869-1110; Christian Scheiwe: 0000-0003-1695-8689; Mukesch J. Shah: 0000-0002-7224-9185; Marcel Heers: 0000-0001-5545-7014; Horst Urbach: 0000-0001-7264-4807; Andreas Schulze-Bonhage: 0000-0003-2382-0506; Marco Prinz: 0000-0002-0349-1955; Ute Häussler: 0000-0001-5601-9833; Andreas Vlachos: 0000-0002-2646-3770; Jürgen Beck: 0000-0002-7687-6098; Julia M. Nakagawa: 0000-0003-1071-5440; Carola A. Haas: 0000-0002-7022-4136

Abstract

Focal cortical dysplasias (FCDs) are local malformations of the human neocortex and a leading cause of intractable epilepsy. FCDs are classified into different subtypes including FCD IIa and IIb, characterized by a blurred gray-white matter boundary or a transmantle sign indicating abnormal white matter myelination. Recently, we have shown that myelination is also compromised in the gray matter of FCD IIa of the temporal lobe. Since myelination is key for brain function, we investigated whether deficient myelination is a feature affecting also other FCD subtypes and brain areas. Here, we focused on the gray matter of FCD IIa and IIb from the frontal lobe. We applied *in situ* hybridization, immunohistochemistry and electron microscopy to quantify oligodendrocytes, to visualize the myelination pattern and to determine ultrastructurally the axon diameter and the myelin sheath thickness. In addition, we analyzed the transcriptional regulation of myelin-associated transcripts by real-time RT-qPCR and chromatin immunoprecipitation (ChIP). We show that densities of myelinating oligodendrocytes and the extension of myelinated fibers up to layer II were unaltered in both FCD types but myelinated fibers appeared fractured mainly in FCD IIa. Interestingly, both FCD types presented with larger axon diameters when compared to controls. A significant correlation of axon diameter and myelin sheath thickness was found for FCD IIb and controls, whereas in FCD IIa large caliber axons were less myelinated. This was mirrored by a down-regulation of myelin-associated mRNAs and by reduced binding-capacities of the transcription factor MYRF to promoters of myelin-associated genes. FCD IIb, however, had significantly elevated transcript levels and MYRF-binding capacities reflecting the need for more myelin due

to increased axon diameters. These data show that FCD IIa and IIb are characterized by divergent signs of maladaptive myelination which may contribute to the epileptic phenotype and underline the view of separate disease entities.

Keywords: neocortex, axon, oligodendrocyte, cortical malformation, epilepsy, chromatin, transcriptional regulation, myelin sheath

Introduction

Focal cortical dysplasias (FCDs) are a frequent cause of pharmcoresistant focal epilepsy, especially in children [1, 2, 3]. Surgical resection of the lesion remains often the only therapeutic option, resulting in a seizure-free clinical outcome in many cases [4, 5]. FCDs comprise a heterogeneous group of cortical malformations morphologically characterized by disturbed lamination and cytoarchitecture including radial and/or horizontal alterations in lamination (FCD Ia or Ib) and the occurrence of dysmorphic neurons (FCD IIa) and/or balloon cells (FCD IIb) [6, 7]. Genetically, sporadic somatic mutations in the *MTOR* (mammalian target of rapamycin) gene and in mTOR pathway-related genes have been identified in FCD IIa and IIb cases leading to hyperactivation of mTOR signaling [8, 9, 10, 11, 12]. Recently, mutations in the GATOR1 complex, a GTPase-activating protein (GAP) complex that regulates TORC1 signaling by interacting with the Rag GTPase, have been found exclusively in FCD IIa of the frontal lobe [13], pointing out pathophysiological differences between FCD IIa and IIb. Accordingly, in the MRI many FCD IIa cases present with a blurring of the gray–white matter boundary [6, 7, 14], whereas FCD IIb shows a funnel-shaped formation through the white matter (WM) (transmantle sign) [15, 16], which is considered as abnormal WM myelination.

Correct myelination is very important for proper brain function and a highly dynamic process involved in memory consolidation in the adult brain [17]. There is recent evidence, that maladaptive myelination does also play a role in epileptic conditions [18, 19]. Indeed, recent reports show a loss of oligodendrocytes (OL) and myelination capacity in the white matter of FCD lesions [14, 20, 21, 22]. Likewise, deficits in myelination were found in the

gray matter of temporal lobe FCDs [23], where impaired proliferation of oligodendrocyte precursor cells (OPC) was part of the FCD pathology [24].

During the differentiation of OPCs into myelinating OLs, a number of transcription factors (TFs) are sequentially expressed to specify the OL fate [25, 26]. Depending on the differentiation stage, these TFs inhibit or stimulate the expression of myelin-associated genes [25]. Oligodendrocyte transcription factor 2 (OLIG2) is a prominent TF that initiates the differentiation of OPCs into myelinating OLs and is expressed across the entire lineage but with decreasing amounts toward the termination of differentiation [27, 28]. A key factor for the completion of OL differentiation is the myelin regulatory factor (MYRF) [29], [30], induced during terminal OL differentiation. MYRF positively regulates the transcription of myelin genes such as myelin basic protein (MBP), 2′, 3′-cyclic nucleotide-3′-phosphodiesterase (CNPase), myelin associated glycoprotein (MAG) and myelin oligodendrocyte glycoprotein (MOG) by binding to their promoters [29, 30].

In the current study, we focused on FCD IIa and IIb in the frontal lobe. There, we investigated the distribution of OLs, the myelination pattern, the ultrastructure of axons and myelin sheaths and the transcriptional regulation of myelin-associated genes in the gray matter. We present evidence for an FCD-type specific dysregulation of myelination: FCD IIa is characterized by a disorganization of the myelin fiber pattern, thinner myelin sheaths of large diameter axons and an attenuation of the myelin synthesis machinery. In contrast, FCD IIb presents with thicker axon diameters and myelin sheaths and an elevated transcriptional turnover of myelin-associated genes.

Methods

Patient Selection

A total of 22 surgically resected frontal lobe specimens from patients with FCD IIa (n=9) [(age at surgery (years): mean: 16.78, range: 6 – 38), (epilepsy duration (years): mean: 10.24, range: 3 – 34)], FCD IIb (n=9) [(age at surgery (years): mean: 33.67, range: 12 – 48), (epilepsy duration (years): mean: 24.33, range: 9 – 41)] and epileptic but non-dysplastic controls (n=4) [approach tissue from tumor resections (WHO grade I) or non-FCD lesions] [(age at surgery (years): mean: 16.75, range: 10 – 26), (epilepsy duration (years): mean: 8, range: 5 – 12)] were included in this study. Individual patients were color-coded to facilitate their identification in the different assays (Table 1).

All cases had undergone neurosurgical interventions due to pharmacoresistant epilepsy or low-grade tumors and removal of cortical tissue was clinically warranted to achieve seizure or tumor control. Pre-surgical assessment included the documentation of a detailed history, neurological examination, neuropsychological testing, MRI scanning and non-invasive/invasive, long-term video EEG monitoring. Informed consent was obtained from all individuals included in the study. All procedures received prior approval by the institutional review board (Ethics Committee, Medical Center - University of Freiburg) and were in accordance with the 1964 Helsinki declaration and its later amendments.

For histopathological diagnosis, all specimens were classified on paraffin sections by the Institute of Neuropathology, Medical Center – University of Freiburg) according to Blümcke et al. (2011) [6].

Tissue Preparation

Brain tissue was collected immediately after resection in ice-cold 0.1M phosphate buffer (PB), pH 7.4. For immunohistochemistry (IHC) and *in situ* hybridization histochemistry (ISHH), slices (~5 mm) were cut perpendicular to the brain's surface, fixed in 4% paraformaldehyde (PFA) [w/v] in PB (24 - 48h, 4°C), cryoprotected in 30% sucrose in PB (24 - 48h, 4°C) and finally stored at -80°C until further processing. For IHC and ISHH, cryostat sections (50 µm, orthogonal to the cortical surface) were prepared, collected in tissue culture dishes, and either rinsed in PB (IHC) or in 2× SSC (1× SSC = 0.15 M NaCl, 0.015 M sodium citrate, pH 7.0) for ISHH.

For electron microscopy (EM), PFA-fixed frozen tissue was cut horizontally to the pia in a cryostat (60 µm) (Leica CM3050 S) and slices were post-fixed in 4% PFA/2.0% glutaraldehyde (GA) in PB (approx. 24h, 4°C) as described previously [23].

For molecular biological techniques the tissue was immediately frozen at -80°C and stored until further processing.

Immunohistochemistry

For NeuN, SMI32 and Vimentin immunolabeling a free-floating protocol was applied. Tissue slices were pretreated in 10% normal serum (NS) and 0.25% Triton X-100 for 30 min at RT and subsequently incubated in 0.1% Triton X-100 and 1% NS in PB with the following primary antibodies: mouse monoclonal anti-NeuN (1:1000; Millipore, #MAB377), anti-SMI32 (specific for non-phosphorylated neurofilament H, 1:1000; Biolegend #801701) and anti-

Vimentin (1:1000; Dako #M0725) at room temperature (RT) overnight. The antibody binding was visualized by incubation with secondary antibodies conjugated with Cyanine (Cy)-3 (1:400; Jackson ImmunoResearch Laboratories) for 2h. Sections were mounted and coverslipped with Immu-Mount (Thermo Scientific).

A modified IHC protocol published by Moreno-Jimerez et al. 2019 [31] was used for the CNPase staining. Tissue sections were incubated in a 0.5% sodium borohydride ($NaBH_4$, Sigma-Aldrich) solution for 30 min at RT. Next, a heat-mediated 10 mM citrate buffer (pH 6.0) antigen retrieval step was performed by boiling the tissue sections in a water bath for 20 min followed by rinsing in 0.1 M PB and pretreatment in 0.5% bovine serum albumin (BSA) and 0.5% Triton for 30 min at RT. Incubation with the CNPase antibody (1:100, Cell Signaling Technology #5664S) was performed under gentle shaking at 4°C for 5 days followed by treatment with the Cy-3-labelled secondary antibody (1:400; Jackson ImmunoResearch Laboratories) for 24h at 4°C under constant shaking. Additionally, all sections were counterstained for 10 min with 4,6-diamidino-2-phenylindole (DAPI,1:10000) to label nuclei. Afterwards, slices were washed three times with PB, mounted on gelatinized microscope slides and treated with an Autofluorescence Eliminator reagent (EMD Millipore) for 5 min following the manufacturer's instructions. Finally, the slices were washed three times with 70% ethanol and coverslipped in aqueous mounting medium (ImmuMount; Thermo Scientific).

In situ Hybridization Histochemistry (ISHH)

Mbp mRNA expression was investigated by ISHH using digoxigenin (DIG)-labeled anti-sense riboprobes, generated from a pBluescript KS II$^+$ vector containing a 1.2 kb *mbp* cDNA as previously described [23].

In brief, cryostat sections (50 µm) were hybridized with a DIG-labeled anti-sense *mbp* cRNA riboprobe (100 ng/ml) at 55°C overnight followed by several stringent washing steps at 65 °C. DIG-labeled hybrids were detected with an anti-DIG antibody from sheep conjugated with alkaline phosphatase as recommended by the manufacturer (Roche) by incubating the slice overnight at 4°C. For signal detection, nitro blue tetrazolium chloride and 5-bromo-4-chloro-3-indolylphosphate were applied and the reaction was developed in the dark. Finally, sections were coverslipped and mounted in Kaiser's gelatin.

Microscopy and Cell counting

Fluorescence and bright field microscopy were performed with an *AxioImager2* microscope (Zeiss) using a 10x (NA 0.45) or 20x (NA 0.75) objective, (both Zeiss). Photomicrographs were taken as tile images with a digital camera (MR605) for fluorescence, AxioCam MRc5 for bright field (both Zeiss), and processed with *Zen* software (Zeiss).

Confocal images were taken using the *Fluoview* FV10i (Olympus) and a 63x oil objective applying the following parameters: image size 1024x1024 pixel, sensitivity 50% and laser power 20% for Cy3 and DAPI. The numerical aperture was selected 1, stacks were taken with 0.5 µm step sizes.

For the quantification *of mbp* mRNA-positive cells, bright field images of three sections per patient were imported into *ImageJ* software. In each image, two regions of interest (ROIs) covering all six cortical layers were defined and within each ROI all digoxigenin-labeled cells were manually counted using the integrated “cell counter” plugin (National Institutes of Health).

For quantitative determination of OL densities, confocal image stacks of CNPase-immunolabled sections were imported into *Image J*. OL cell bodies were counted in three slices per patient and in each slice three ROIs of the cortical layers V/VI (9 ROIs/patient) were manually counted by starting from the first image, where cells appeared and stopped at the last countable image. Cell numbers were related to the volume of the counted stacks and given as a mean over all ROIs per patient (cell number/mm^3).

Electron Microscopy

For electron microscopy, slices were cut perpendicular to the pia from the fixed, frozen block (60µm) and post-fixed in the presence of 4% PFA and 2% glutaraldehyde for 24h at 4°C as described before [24]. Some sections were stained with 1% cresyl violet to visualize the cortical layers, required for orientation before embedding. The other slices were osmicated for 2 h with 1% osmium tetroxide in 6.86% sucrose in PB, subsequently contrasted with 1% uranyl acetate in 70% ethanol overnight at 4°C and dehydrated in graded ethanol. The cortical gray matter was flat-embedded in epoxy resin (Durcupan ACM, Sigma-Aldrich), which was polymerized overnight. Ultrathin sections (60 nm) in the horizontal plane were prepared with an ultramicrotome (LEICA

UC6) and collected on copper grids. Sections were analyzed with a TEM LEO 906E (Zeiss). Electron photomicrographs of layers V/VI were taken with the CCD-Camera “sharp eye” (Tröndle) and visualized with ISP software (Tröndle).

For quantitative analysis images were imported into *ImageSP* (TRS & SYSPROG). With this software the outer and the inner diameter of myelinated relation of the axon diameter to the total fiber diameter [32], was calculated.

RNA Isolation, Reverse Transcription and Real-Time RT-qPCR Analysis

The isolation of total RNA, reverse transcription, and real-time qPCR was performed as described earlier [23]. In brief, frozen specimens were thawed on ice and the white matter was carefully removed with a scalpel in *RNAlater* (Qiagen). The total RNA was isolated from 30 mg cortical gray matter using the *RNeasy Mini kit* (Qiagen) according to the manufacturer’s guidelines. Afterwards, a reverse transcription (RT) step was carried out with 1µg total RNA per reaction using the *First Strand cDNA Synthesis Kit* (ThermoFisher Scientific).

The expression of mRNAs was quantified by real-time RT-qPCR on a *CFX Connect™* Real-Time PCR System (Bio-Rad Laboratories) in the presence of *SsoAdvanced universal SYBR Green Mix* (Bio-Rad Laboratories). The following human-specific primer pairs were used at 70 nM: *s12* (mitochondrial ribosomal protein S12) (forward (f): 5’-AGTTGGTGGAGGCCCTTTGT-3’, reverse (r): 5’-AGGCCTACCCATTCTCCTAGTTTC-3’), *mbp* (f: 5’-AATTACTCACCGAGACACAC-3’, r: 5’-GAAGGATATGGTCAGAAGAG-3’),

mag (f: 5'-CAACTGAGTCCAAGTTGTCT-3', r: 5'-ATTCTGTACAGCGAGTGAGT-3'), *mog* (f: 5'-CTTCGAGCAGAGATAGAGAA-3', r: 5'-TCGATGTAGCCAGTTGTAG-3'), *myrf* (f: 5'-CTACCACATCCCTGTCAGT-3', r: 5'-GGAGGAGGAGTTCATCTG-3'), CNP (f: 5'-ACACACAGCTTCTAGTGATTT-3', r: 5'-ACAGAGAAGCGAGTTCAG-3'), *olig2* (f: 5'-AATCTCAATATCTGGGTC AA-3', r: 5'-GGAACATCCACAGATTTATT-3'), *sip1* (Smad interacting protein 1) (f: 5'-AGCCTCTGTAGATGGTCCAGAAGAA-3', r: 5'-GCGGTCTGGATCGTGGCTTC-3').

The PCR conditions were chosen as published before [23]. The resulting Ct (cycle threshold) values (obtained by the CFX Manager™ Software, Bio-Rad Laboratories) were used to calculate relative expression levels for genes of interest by normalization to the housekeeping gene S12.

Chromatin immunoprecipitation (ChIP)

The ChIP assays were performed using the *iDeal ChIP-seq* kit for transcription factors (Diagenode) with fresh-frozen FCD and control tissue (30 mg per IP) according to manufacturer's guidelines. Firstly, the gray matter was manually dissected and homogenized with 1% formaldehyde to cross-link genomic DNA and proteins for 15 min at RT. The chromatin lysate was sonicated and chromatin was fragmented to a size of approx. 500-1000 base pairs using the *Bioruptor® Pico* (Diagenode) by running 10 cycles with settings 30 sec. on, 30 sec. off per cycle. To reduce non-specific binding, we included a preclearing step by incubating the chromatin lysate with *DiaMag* Protein A-coated magnetic beads (Diagenode) at 4°C for 1.5 - 2 hours, Next,

the chromatin was precipitated with polyclonal rabbit MYRF (5 µg, Millipore), and polyclonal goat OLIG2 (5 µg, R&D) antibodies, all pre-incubated for 4h at 4°C with Protein A-coated magnetic beads, and non-specific polyclonal rabbit IgG (1 µg, Diagenode), overnight at 4°C under constant rotation. Afterwards, the chromatin was stringently washed, eluted from the beads and the crosslinking was reversed by incubating the eluate at 65°C overnight. Subsequently, the DNA was purified using *IPure beads v2* (Diagenode) eluted with H_2O and stored at -20°C until further use.

ChIP specificity was verified by real-time qPCR for known transcription factor binding sites (e.g., *MAG*; *MOG*, *MBP*). The PCR primers were designed around predicted transcription factor binding sites (BS), which were identified by using the *MatInspector* tool form *Genomatix* software. Using this tool, we detected the following transcription factor BS sequences: *MBP* (MYRF BS): 5'-TTTCCTGGTACAT-3', *SIP 1* (OLIG2 BS): 5'-AGGCCAGCTGTTTCA-3', *CNP* (OLIG2 BS): 5'-AGCCCCAGCTGCTCTG-3' and *MBP* (OLIG2 BS): 5'-AAAGCAGCTGCCTGG-3'. The following primers were used for ChIP-qPCR analysis: *MBP* (MYRF ChIP): (f: 5'-GTCTGCTTGTCTGTTTCCCA-3', r: 5'-TCCGGGGATTGACTTTCAGA-3'), *SIP1* (OLIG2 ChIP): (f: 5'-TCCTCATGGAACTTGAGTCG-3', r: 5'-AAAACCCTGATATCCTGACAGC-3'), *CNP* (OLIG2 ChIP): (f: 5'-GAA CCTGGACCAAAGCTGAC-3', r: 5'-TCTGAGGTGTCTCCCCACTC-3') and *MBP* (OLIG2 ChIP): (f: 5'-TCGTGTGCAGTGCTTAGACC-3', r: 5'-TTTCATTCAGCCTGTGCTTG-3'). The PCR was run with the following conditions: 1. Hotstart: 3 min 95°C, 2. Amplification: 30 sec 95°C, 30 sec 63°C, 30 sec 72°C (40 cycles). ChIP-qPCR was analyzed by calculating the relative amount of immunoprecipitated

DNA compared to INPUT DNA for the control regions (% of recovery) using the following formula: % recovery = $2^{[(Ct_{input} – 6.64) - Ct_{sample})]} \times 100\%$.

Statistical analysis

Prism 8 software (GraphPad Software Inc.) was used for statistical analysis. For all experimental values, mean and standard error of the mean (SEM) are given. Shapiro-Wilk normality test was applied for distribution testing. Group comparisons were performed with one-way ANOVA or Kruskal-Wallis test and Tukey's or Dunn's multiple comparison post hoc test. Significance thresholds were set to: *P < 0.05, **P < 0.01, ***P < 0.001. Correlations of axon diameter with myelin sheath thickness, g-ratio and mRNA expression levels with transcription factor binding capacities were tested using Pearson's correlation. Data for group comparisons for cumulative frequencies were tested for normality and logarithmically transformed before applying the one-way ANOVA and Tukey's multiple comparison post hoc test.

Results

MR imaging and histopathological analysis of FCD type II cases

All patients included in this study were scanned by MRI with either FLAIR- or STIR-weighted sequences according to a standard protocol to detect potential lesions [33, 34, 35]. The FCD IIa group was heterogeneous with respect to a detectable lesion: five patients showed a thickening of the cortex and blurring of the gray-white matter boundary (Fig. 1a, b), one case had a transmantle sign and three were MRI-negative (Table 1). In contrast, all patients of the

FCD IIb cohort presented with a transmantle sign, a zone of increased signal intensity tapering toward the lateral ventricle (Fig. 1c, d; Table 1).

Since FCDs can be variable in extensions and dimensions, we characterized every resected specimen included in this study regarding the lamination pattern and cytoarchitecture and determined the FCD type according to the ILAE classification [6]. To this end, serial sections of all cases were stained with cresyl violet and were immunolabeled for NeuN to visualize all layers, or for SMI32, a monoclonal antibody specific for non-phosphorylated neurofilament H [36], which labels pyramidal cells of layers III and V.

In controls, all six cortical layers were present as shown by Nissl staining or NeuN labeling (Fig. 2a, b). Pyramidal cells in layers III and V appeared normally shaped with parallel-orientated apical dendrites, which reached the border of layer I (Fig. 2c). In the FCD IIa cohort, Nissl and NeuN stainings showed a mild hypercolumnization across layers II to V (Fig. 2d, e). Moreover, the occurrence of dysmorphic neurons, characterized by malorientation and the strong accumulation of non-phosphorylated neurofilament was apparent, in particular, in layers III and V/VI (Fig. 2f, j). FCD IIb cases were characterized by blurring of the cortical layers (Fig. 2g, h), the presence of dysmorphic neurons in all layers and at the gray-white matter boundary (Fig. 2i, k). Balloon cells, characteristic for FCD IIb, were recognizable in the cortical white matter by vimentin labeling (Fig. 2l).

Altogether, by applying presurgical MRI and histological characterization of all specimens, we ensured the characteristic phenotype of the two FCD cohorts and of the control group.

Distribution of myelinating OLs in the gray matter of the frontal lobe

Inspired by our pervious results from the temporal lobe, where we had found FCD-associated myelination deficits and reduced numbers of myelinating OLs [23, 24], we started the analysis of myelination in frontal lobe FCD IIa and IIb with studying the distribution of mature OLs, the myelin-producing cells. To this end, we performed ISHH for *mbp* mRNA, which is exclusively expressed in mature, myelinating oligodendrocytes [37] (Fig. 3). In controls, *mbp* mRNA-expressing OLs were most numerous in the infragranular layers of the gray matter and thinned out gradually up to layer I (Fig. 3b, c). In FCD IIa, less OLs were detectable; some, located in the deep cortical layers, exhibited very strong *mbp* mRNA signals (Fig. 3e, f). In contrast, in FCD IIb *mbp* mRNA-expressing OLs appeared slightly more numerous across the entire cortex when compared to controls and FCD IIa cases (Fig. 3h, i). However, counting of *mbp*-positive cells did not reveal any significant differences between controls, FCD IIa and FCD IIb [controls (n=4): 178.9 ± 42.1 cells/mm²; FCD IIa (n=7) 129.8 ± 24.9 cells/mm²; FCD IIb (n=7): 246.9 ± 43.4 cells/mm^2; (one-way ANOVA F=2.64, p=0.106)] (Fig. 3j).

Altogether, in contrast to the temporal lobe, the density of myelinating OLs was unaltered in FCD type II of the frontal lobe.

Myelination pattern and ultrastructure of myelinated axons in the gray matter

To investigate the architecture of myelinated fibers in the gray matter of control and FCD type II specimens we used immunolabeling for CNPase, a marker for pre-OLs, mature OLs and myelin [38].

In control tissue, a dense, radially aligned network of CNPase-positive myelinated fibers extended from the gray-white matter boundary up to layer III, declining gradually from the white matter to the upper layers (Fig. 4a). In FCD IIa and IIb, a similar pattern of CNPase-immunolabeled fibers was observed, reaching up to layer III as in the non-dysplastic cortex (Fig. 4b, c). High resolution confocal imaging in layers V/VI demonstrated radially aligned fibers in the control case and in FCD IIb (Fig. 4d, f) but disorganized and fractured strands in FCD IIa (Fig. 4e). Counting of CNPase-labelled pre-OL and OL cell bodies across all layers did not reveal any significant differences between controls, FCD IIa and FCD IIb cases [controls (n=4): 34380 ± 3259 cells/mm^3; FCD IIa (n=9) 38674 ± 5211 cells/mm^3; FCD IIb (n=9): 44580 ± 5457 cells/mm^3; (one-way ANOVA F=0.74, p=0.49)] (Fig. 4g).

Next, we compared the ultrastructure of myelinated axons of control and FCD cases by transmission electron microscopy in layers V/VI (Fig. 5a-c), where axons show a high and homogeneous myelin coverage [39]. We determined the axon diameter, the myelin sheath thickness and the g-ratio, defined as the ratio of the axon diameter to the total fiber diameter [32].

Mean axon diameters were slightly increased in both FCD cohorts when compared to the control group [(axon diameters: control: 323.9 ± 27.7 nm; FCD IIa: 424.8 ± 23.8 nm; FCD IIb: 436.1 ± 55.5 nm); (one-way ANOVA F=2.59, p=0.129)] (Fig. 5d). When we looked at the frequency distribution of all axon diameters within each group, we found a significant shift towards larger axon diameters in both FCD types [controls (n=4; 114 axons) 119.9.8 – 767.5 nm; FCD IIa (n=4; 192 axons) 129.5 – 1141.5 nm; FCD IIb (n=4; 116 axons) 151.4 – 1346.2 nm] (one-way ANOVA F=19.26, p<0.0001; Tukey's

post hoc test: control vs. FCD IIa $p<0.0001$, control vs. FCD IIb $p<0.0001$, FCD IIa vs. FCD IIb $p=0.691$)] (Fig. 5e). The mean g-ratio of myelinated axons was elevated in FCD IIb and significantly increased in FCD IIa when compared to non-dysplastic controls [(g-ratios: control: 0.698 ± 0.008; FCD IIa: 0.744 ± 0.017; FCD IIb: 0.728 ± 0.012); (one-way ANOVA $F=4.511$, $p=0.044$; Tukey's post hoc test: control vs. FCD IIa $p=0.039$, control vs. FCD IIb $p=0.174$, FCD IIa vs. FCD IIb $p=0.611$)] (Fig. 5f). This was even more prominent when we looked at the relative frequency distribution of all g-ratio values: both FCD II groups had significantly increased g-ratios in comparison to the control group and FCD IIa showed significantly higher values than FCD IIb [(one-way ANOVA $F=14.69$, $p<0.0001$; Tukey's post hoc test: control vs. FCD IIa $p<0.0001$, control vs. FCD IIb $p=0.019$, FCD IIa vs. FCD IIb $p=0.046$)] (Fig. 5g). Normally, an increased g-ratio indicates a reduced thickness of the myelin sheath, based on the assumption that the axon diameters are not altered. However, since our FCD cases had significantly larger axon diameters, we investigated also the myelin sheath thicknesses. On average, there was no difference between the three groups [(myelin sheath thickness: control: 133.5 ± 12.39 nm; FCD IIa: 132.7 ± 4.312 nm; FCD IIb: 147.3 ± 9.828 nm); (one-way ANOVA $F=0.746$, $p=0.501$)] (Fig. 5h). However, plotting the relative frequency distribution of all individual values revealed that FCD IIb had significantly thicker myelin sheaths when compared to controls and FCD IIa cases [(one-way ANOVA $F=4.487$, $p=0.012$; Tukey's post hoc test: control vs. FCD IIa $p= 0.941$, control vs. FCD IIb $p=0.023$, FCD IIa vs. FCD IIb $p=0.024$)] (Fig. 5i) but also thicker axons than controls.

So solve this controversy, we correlated all individual axon diameters with the corresponding myelin sheath thickness for the three groups separately: (in nm): controls (range: smallest axon diameter/myelin sheath 119.92/91.59; largest axon diameter/myelin sheath 767.5/130.77); FCD IIb (range: smallest axon diameter/myelin sheath 151.41/103.22, largest axon diameter/myelin 1346.19/146.09). We found significant correlations between axon diameter and myelin sheath thickness in controls (Pearson's correlation: r=0.329, p=0.0003) and FCD IIb (Pearson's correlation: r=0.309, p=0.0007) (Fig. 5j, l), implying that the axon caliber determines the thickness of the myelin sheath [40]. This was not the case for FCD IIa (Pearson's correlation: r=0.138, p=0.056) (range: smallest axon diameter/myelin sheath 129.48/124.41, largest axon diameter/myelin sheath 1141.5/92.95), where large caliber axons (above 700 nm) had thinner myelin sheaths than axons of the same caliber in controls or FCD IIb (Fig. 5k) indicating that myelination was selectively compromised for axons with a large diameter in FCD IIa.

Transcriptional regulation of OL differentiation factors and myelin-associated genes

Since thinner myelin sheaths may indicate a disturbance in OL differentiation and/or myelin synthesis, we next tested whether the transcriptional regulation of OL differentiation and myelination was affected in our FCD cohorts. First, we performed real-time RT-qPCR to measure the mRNA levels of transcription factors either sequentially active at different stages of OL maturation (SIP1, MYRF) or continuously expressed (OLIG2). In addition, we

quantified the expression levels of *mbp*, *mag* and *mog* mRNA, which encode proteins that are all components of the myelin sheath.

Olig2 (Kruskal-Wallis p=0.793) and *sip1* (one-way ANOVA F=0.648, p=0.534) mRNA levels were similar in all groups (Fig. 6a, b), whereas *myrf* mRNA expression was significantly down-regulated in FCD IIa when compared to FCD IIb (one-way ANOVA F=7.914, p=0.003; Tukey's post hoc test: control vs. FCD IIa p=0.389, control vs. FCD IIb p=0.205, FCD IIa vs. FCD IIb p=0.002) (Fig. 6c). Likewise, *mbp* (one-way ANOVA F=5.964, p=0.009; Tukey's post hoc test: control vs. FCD IIa p= 0.672, control vs. FCD IIb p=0.190, FCD IIa vs. FCD IIb p=0.008), *mag* (one-way ANOVA F=11.46, p=0.0005; Tukey's post hoc test: control vs. FCD IIa p=0.288, control vs. FCD IIb p=0,099, FCD IIa vs. FCD IIb p=0.0004), and *mog* (one-way ANOVA F= 7.551, p=0.004; Tukey's post hoc test: control vs. FCD IIa p=0.163, control vs. FCD IIb p=0.515, FCD IIa vs. FCD IIb p=0.003), mRNA levels were also significantly decreased in FCD IIa in comparison to FCD IIb (Fig. 6d-f) reflecting the regulatory action of MYRF on myelin genes.

To target the level of transcriptional regulation directly, we next performed ChIP assays which give insight into transcription factor binding to specific promoters. Chromatin was purified from gray matter of control, FCD IIa and IIb specimens and immunoprecipitated with antibodies specific for transcription factors which either determine the OL lineage (OLIG2) or the advanced differentiation stage (MYRF). As transcription factor targets, we chose either genes encoding transcription factors (*SIP1, SOX10*) or structural proteins of the myelin sheath (*MBP*, *MAG*, *MOG*, *CNP*) and quantified the

OLIG2 and MYRF binding capacities to the predicted binding sites by real-time qPCR.

We did not find any differences in the binding capacities of OLIG2 to the *SIP1* (one-way ANOVA F=0.153, p=0,859), *MBP* (one-way ANOVA F=0.247, p=0.784), *CNP* (one-way ANOVA F=0.654, p=0.531) and *MOG* (Kruskal-Wallis p=0.475) promoters between control (n=4), FCD IIa (n=9) and FCD IIb (n=9) cases indicating that OLIG2 is equally active in the different groups (Fig. 7a-d). In contrast, MYRF showed a significantly decreased affinity to the *SOX10* (one-way ANOVA F=10.51, p=0.0008; Tukey's post hoc test: control vs. FCD IIa p=0.0009, control vs. FCD IIb p= 0.112, FCD IIa vs. FCD IIb p= 0.024), *MBP* (one-way ANOVA F=6.55, p=0.007; Tukey's post hoc test: control vs. FCD IIa p=0.032, control vs. FCD IIb p= 0.976, FCD IIa vs. FCD IIb p= 0.011) and *MAG* (Kruskal-Wallis p=0.003; Dunn's multiple comparison test: control vs. FCD IIa p=0.017, control vs. FCD IIb p>0.999, FCD IIa vs. FCD IIb p=0.041) promoters in FCD IIa specimens when compared to FCD IIb or controls (Fig. 7e-g) indicating an FCD IIa-specific transcriptional dysregulation of myelin-associated genes.

Finally, we tested, whether there is a direct impact of the investigated transcription factor binding capacities on the corresponding mRNA expressions. We correlated the promoter binding capacities of OLIG2 and MYRF with the corresponding *sip1*, *mbp*, *mog*, and *mag* mRNA levels. There were no differences in the promoter binding capacities of OLIG2 to their target promoters (data not shown). However, we found a significant correlation of the MYRF binding capacity with expression levels of *mbp* (Pearson's correlation: r=0.546, p=0.009) and *mag* (Pearson's correlation: r=0.539,

p=0.009) transcripts in FCD IIb but less in FCD IIa (Fig. 7h, i) mirroring the low expression of myelin-associated genes in FCD IIa.

Discussion

Insulation of axons by myelin is important for fast and long-range signal propagation in the brain. Myelin is constantly produced in the adult brain by oligodendrocytes in a plasticity-dependent manner and necessary for memory consolidation [17]. Myelination deficiencies have been found in several neurologic disorders in particular in multiple sclerosis [41] and are often associated with seizure occurrence [42]. There is increasing awareness that also in epilepsy maladaptive myelination or axon demyelination are of high relevance for seizure generation [19, 18].

In this study, we investigated maladaptive myelination and the transcriptional regulation of myelin-associated genes in FCD specimens obtained from patients with pharmacoresistant focal epilepsy. We focused on the gray matter of FCD IIa and IIb cases from the human frontal lobe, all thoroughly characterized by presurgical MR scans and *post hoc* histological analysis. In the MRT, most FCD IIa patients showed a thickening of the neocortex and blurring of the gray-white matter boundary, whereas all FCD IIb cases displayed a transmantle sign [15]. Histological characterization ensured that all specimens of our study fulfilled the morphological criteria proposed by the ILAE [6, 7].

The extension of radially orientated, myelinated CNPase-positive fibers, was similar in FCD cases and controls, reaching up to layer III as described earlier for the temporal cortex [43, 24]. However, high resolution

confocal microscopy in layer V/VI revealed fractured and distorted myelinated axons mainly in FCD IIa specimens, in line with our previous study in the gray matter of the temporal lobe [23].

When we analyzed myelinated axons ultrastructurally and determined axon diameter, myelin sheath thickness and g-ratio, we found a significantly increased g-ratio for FCD IIa cases, pointing to a reduced thickness of the myelin sheath as found in the temporal lobe [24]. However, the frequency distribution of axon diameters indicated a significant increase of axon calibers in both FCD cohorts in comparison to controls. Unfortunately, there is hardly any information about the physiological range of axon diameters in the human gray matter, since most studies focused on fiber tracts in the white matter. Liewald et al. [44] reported a frequency distribution of 300 – 1500 nm for axon diameters in the human white matter. We found much thinner axons (119 – 767 nm) in controls but both FCD cohorts approached values (FCD IIa: 130 – 1142 nm; FCD IIb: 151 – 1346 nm) similar to those reported by Liewald et al. [44]. Since the axon diameter depends strongly on the soma size of the parent neuron [45], it is tempting to speculate that the presence of large dysmorphic neurons, being part of the FCD II pathology, could be the reason for larger axon diameters in our FCD cases in comparison to control tissue.

Since the axon diameter is critical for the calculation of the g-ratio [32], we performed a more refined analysis of all individual values and correlated the corresponding axon diameters and myelin sheath thicknesses. We found a clear correlation of both parameters in FCD IIb and controls, showing a linear relationship between axon diameter and myelin sheath thickness as reported in the literature [40]. This was not the case in FCD IIa specimens,

where large diameter axons (≥ 700 nm) had thinner myelin sheaths than corresponding axons of FCD IIb and controls indicating a myelination deficiency of large diameter axons only in the FCD IIa cohort.

What could be the explanation for thinner myelin sheaths in FCD IIa? It might be that the differentiation of OLs, the myelin sheath-producing glial cells, and their myelin-synthesizing capacities are compromised. In fact, a loss of OPCs and OLs [14, 21] and decreased myelin synthesis, shown in an *in vitro* myelination assay [22] has been demonstrated for the white matter of FCD cases. Similarly, we had found significantly less OPCs and a reduced proliferation capacity of OPCs purified from the gray matter of temporal FCD IIa [24].

In the current study, we did not find altered numbers of *mbp* mRNA- or CNPase-positive pre-OLs and OLs in both FCD II types suggesting that the OL lineage is basically preserved in the dysplastic gray matter of the frontal lobe. This was supported by constant levels of *olig2* and *sip1* mRNA, which encode transcription factors required for the maturation of OLs [46, 47] and by unaltered binding capacities of OLIG2 to genes encoding structural myelin proteins as shown in our ChIP assays.

Alternatively, the mature OL population might have an impaired myelination capacity in FCD type II. Indeed, we found significantly reduced *myrf* mRNA levels in FCD IIa pointing to an attenuation of myelin production in mature OLs of this FCD type. MYRF is a key component of the transcriptional regulatory network responsible for the induction and maintenance of the myelinating OL phenotype [48]. Accordingly, myelin-associated genes such as *MBP*, *MAG* and *MOG* were significantly down-regulated in FCD IIa specimens

in comparison to FCD IIb. The latter had even higher mRNA levels of myelin components than controls, in agreement with an elevated need for myelin proteins due to thicker axons and myelin sheaths. This was also reflected on the level of transcriptional regulation analyzed by our ChIP assays: all investigated promotor-binding capacities of MYRF to the SOX10, MBP and MAG promoters were significantly elevated in FCD IIb when compared to FCD IIa indicating an enhanced myelin production. This was further supported by the significant correlation between MYRF promotor binding capacities and *mag* and *mbp* mRNA levels. Altogether, our results point to divergent forms of maladaptive myelination in FCD IIa and IIb.

What are the functional effects of an impaired myelination? Under physiological conditions, myelination depends strongly on neuronal activity [49]. In rodents, there is recent evidence that neuronal activity increases OL differentiation and myelin sheath thickness in a pathway-specific manner [50]. Accordingly, Knowles et al. [18] found increased oligodendrogenesis and myelination in an animal model for absence seizures and demonstrated that it contributes to epilepsy progression. In contrast, we found in our human FCD IIa cases thinner myelin sheaths in layer V/VI of the temporal lobe [24] and, as shown here, of the frontal lobe. We did not find any correlation with seizure frequency or duration (data not shown) indicating that different epilepsy types result in different forms of maladaptive myelination.

CONCLUSIONS

Our study demonstrates for the first time that there is a dysregulation of myelination in the gray matter of frontal lobe FCD IIa and FCD IIb. Both FCD

types show divergent signs of maladaptive myelination: FCD IIa is characterized by a disorganization of the myelin fiber pattern, thinner myelin sheaths of large diameter axons and an attenuation of the myelin synthesis machinery. In contrast, FCD IIb presents with thicker axon diameters and myelin sheaths and an elevated transcriptional turnover of myelin-associated genes. This imbalance in myelination may disrupt the equilibrium of signal conduction and thereby contribute to the epileptic phenotype.

Abbreviations

ChIP: Chromatin immunoprecipitation

CNPase: 2',3'-cyclic nucleotide 3'-phosphodiesterase

EM: Electron microscopy

FCD: Focal cortical dysplasia

IHC: Immunohistochemistry

ISHH: *In situ* hybridization histochemistry

MAG: Myelin-associated glycoprotein

MBP: Myelin basic protein

MOG: Myelin oligodendrocyte glycoprotein

MRI: Magnetic resonance imaging

MTOR: mammalian target of rapamycin

MYRF: Myelin regulatory factor

OL: Oligodendrocyte

OLIG2: Oligodendrocyte transcription factor 2

OPC: Oligodendrocyte precursor cell

PB: phosphate buffer

SIP1: Smad interacting protein 1

SOX10: SRY-box transcription factor 10

TF: Transcription factor

Declarations

Ethics approval and consent to participate

All procedures received prior approval by the institutional review board (Ethics Committee, Medical Center - University of Freiburg) and were in accordance with the 1964 Helsinki declaration and its later amendments. Informed consent was obtained from all individuals included in the study.

Availability of data and material

The data that support the findings of this study are available from the corresponding author upon written request.

Competing interest

The authors declare no conflict of interest.

Funding

German Research Foundation (grant number: DO 2542/1-1), Research Commission, Medical Faculty - University of Freiburg (grant DON 1207/19).

Authors' contributions

CD: Conceptualization; data curation; formal analysis; project administration; visualization; writing - original draft; funding acquisition; SH: Visualization;

formal analysis; CS, MJS: Neurosurgical brain resection; TD, MH, ASB, HU, MP, JB: Clinical data; UH: Statistical analysis; commenting manuscript; AV: Electron microscopy; JMN: Brain resection, clinical data from patients; CAH: Conceptualization; data interpretation, manuscript writing, resources.

Acknowledgement

We thank all the patients who donated tissue for this study. We are grateful to Sigrun Nestel for excellent technical assistance and to Dr. Maria Stella Carro for help with establishing the chromatin immunoprecipitation method.

References

1. Palmini A, Andermann F, Olivier A, Tampieri D, Robitaille Y, Andermann E, et al. Focal neuronal migration disorders and intractable partial epilepsy: A study of 30 patients. Ann. Neurol. 1991;30:741–9.

2. Fauser S, Schulze-Bonhage A, Zentner J. Focal cortical dysplasias: surgical outcome in 67 patients in relation to histological subtypes and dual pathology. Brain. 2004;127:2406–18.

3. Fauser S, Huppertz H-J, Schulze-Bonhage A. Clinical characteristics in focal cortical dysplasia: a retrospective evaluation in a series of 120 patients. Brain. 2006;129:1907–16.

4. Zhao B, Zhang C, Wang X, Wang Y, Liu C, Mo J, et al. Sulcus-centered resection for focal cortical dysplasia type II: surgical techniques and outcomes. J. Neurosurg. 2020;135:266–72.

5. Willard A, Antonic-Baker A, Chen Z, O'Brien TJ, Kwan P, Perucca P. Seizure Outcome After Surgery for MRI-Diagnosed Focal Cortical Dysplasia: A Systematic Review and Meta-analysis. Neurology [Internet]. 2022 [cited 2024 Jan 29];98. Available from: https://www.neurology.org/doi/10.1212/WNL.0000000000013066

6. Blümcke I, Thom M, Aronica E, Armstrong DD, Vinters HV, Palmini A, et al. The clinicopathologic spectrum of focal cortical dysplasias: A consensus classification proposed by an ad hoc Task Force of the ILAE Diagnostic Methods Commission1: The ILAE Classification System of FCD. Epilepsia. 2011;52:158–74.

7. Najm I, Lal D, Alonso Vanegas M, Cendes F, Lopes-Cendes I, Palmini A, et al. The ILAE consensus classification of focal cortical dysplasia: An update proposed by an ad hoc task force of the ILAE diagnostic methods commission. Epilepsia. 2022;63:1899–919.

8. Abdijadid S, Mathern GW, Levine MS, Cepeda C. Basic Mechanisms of Epileptogenesis in Pediatric Cortical Dysplasia. CNS Neurosci Ther. 2015;21:92–103.

9. Lim JS, Kim W, Kang H-C, Kim SH, Park AH, Park EK, et al. Brain somatic mutations in MTOR cause focal cortical dysplasia type II leading to intractable epilepsy. Nat Med. 2015;21:395–400.

10. Baldassari S, Ribierre T, Marsan E, Adle-Biassette H, Ferrand-Sorbets S, Bulteau C, et al. Dissecting the genetic basis of focal cortical dysplasia: a large cohort study. Acta Neuropathol. 2019;138:885–900.

11. Nguyen LH, Mahadeo T, Bordey A. mTOR Hyperactivity Levels Influence the Severity of Epilepsy and Associated Neuropathology in an Experimental Model of Tuberous Sclerosis Complex and Focal Cortical Dysplasia. J Neurosci. 2019;39:2762–73.

12. Chung C, Yang X, Bae T, Vong KI, Mittal S, Donkels C, et al. Comprehensive multi-omic profiling of somatic mutations in malformations of cortical development. Nat Genet. 2023;55:209–20.

13. Honke J, Hoffmann L, Coras R, Kobow K, Leu C, Pieper T, et al. Deep histopathology genotype–phenotype analysis of focal cortical dysplasia type II differentiates between the GATOR1-altered autophagocytic subtype IIa and MTOR-altered migration deficient subtype IIb. Acta Neuropathol. Commun. 2023;11:179.

14. Mühlebner A, Coras R, Kobow K, Feucht M, Czech T, Stefan H, et al. Neuropathologic measurements in focal cortical dysplasias: validation of the

ILAE 2011 classification system and diagnostic implications for MRI. Acta Neuropathol. 2012;123:259–72.

15. Urbach H, Scheffler B, Heinrichsmeier T, Von Oertzen J, Kral T, Wellmer J, et al. Focal Cortical Dysplasia of Taylor's Balloon Cell Type: A Clinicopathological Entity with Characteristic Neuroimaging and Histopathological Features, and Favorable Postsurgical Outcome. Epilepsia. 2002;43:33–40.

16. Kimura Y, Shioya A, Saito Y, Oitani Y, Shigemoto Y, Morimoto E, et al. Radiologic and Pathologic Features of the Transmantle Sign in Focal Cortical Dysplasia: The T1 Signal Is Useful for Differentiating Subtypes. AJNR Am J Neuroradiol. 2019;40:1060–6.

17. Steadman PE, Xia F, Ahmed M, Mocle AJ, Penning ARA, Geraghty AC, et al. Disruption of Oligodendrogenesis Impairs Memory Consolidation in Adult Mice. Neuron. 2020;105:150-164.e6.

18. Knowles JK, Xu H, Soane C, Batra A, Saucedo T, Frost E, et al. Maladaptive myelination promotes generalized epilepsy progression. Nat Neurosci. 2022;25:596–606.

19. De Curtis M, Garbelli R, Uva L. A hypothesis for the role of axon demyelination in seizure generation. Epilepsia. 2021;62:583–95.

20. Shepherd C, Liu J, Goc J, Martinian L, Jacques TS, Sisodiya SM, et al. A quantitative study of white matter hypomyelination and oligodendroglial maturation in focal cortical dysplasia type II. Epilepsia. 2013;54:898–908.

21. Scholl T, Mühlebner A, Ricken G, Gruber V, Fabing A, Samueli S, et al. Impaired oligodendroglial turnover is associated with myelin pathology in focal cortical dysplasia and tuberous sclerosis complex. Brain Pathol. 2017;27:770–80.

22. Gruber V, Lang J, Endmayr V, Diehm R, Pimpel B, Glatter S, et al. Impaired myelin production due to an intrinsic failure of oligodendrocytes in mTORpathies. Neuropathol. Appl. Neurobiol. 2021;47:812–25.

23. Donkels C, Pfeifer D, Janz P, Huber S, Nakagawa J, Prinz M, et al. Whole Transcriptome Screening Reveals Myelination Deficits in Dysplastic Human Temporal Neocortex. Cereb Cortex. 2016;bhv346.

24. Donkels C, Peters M, Fariña Núñez MT, Nakagawa JM, Kirsch M, Vlachos A, et al. Oligodendrocyte lineage and myelination are compromised in the gray matter of focal cortical dysplasia type IIa. Epilepsia. 2020;61:171–84.

25. Emery B. Regulation of Oligodendrocyte Differentiation and Myelination. Science. 2010;330:779–82.

26. Sock E, Wegner M. Using the lineage determinants Olig2 and Sox10 to explore transcriptional regulation of oligodendrocyte development. Dev. Neurobiol. 2021;81:892–901.

27. Mei F, Wang H, Liu S, Niu J, Wang L, He Y, et al. Stage-Specific Deletion of Olig2 Conveys Opposing Functions on Differentiation and Maturation of Oligodendrocytes. J Neurosci. 2013;33:8454–62.

28. Meijer DH, Sun Y, Liu T, Kane MF, Alberta JA, Adelmant G, et al. An Amino Terminal Phosphorylation Motif Regulates Intranuclear Compartmentalization of Olig2 in Neural Progenitor Cells. J Neurosci. 2014;34:8507–18.

29. Emery B, Agalliu D, Cahoy JD, Watkins TA, Dugas JC, Mulinyawe SB, et al. Myelin Gene Regulatory Factor Is a Critical Transcriptional Regulator Required for CNS Myelination. Cell. 2009;138:172–85.

30. Bujalka H, Koenning M, Jackson S, Perreau VM, Pope B, Hay CM, et al. MYRF Is a Membrane-Associated Transcription Factor That Autoproteolytically Cleaves to Directly Activate Myelin Genes. ffrench-Constant C, editor. PLoS Biol. 2013;11:e1001625.

31. Moreno-Jiménez EP, Flor-García M, Terreros-Roncal J, Rábano A, Cafini F, Pallas-Bazarra N, et al. Adult hippocampal neurogenesis is abundant in neurologically healthy subjects and drops sharply in patients with Alzheimer's disease. Nat Med. 2019;25:554–60.

32. Rushton WAH. A theory of the effects of fibre size in medullated nerve. J. Physiol. 1951;115:101–22.

33. Urbach H, Mast H, Egger K, Mader I. Presurgical MR Imaging in Epilepsy. Clin Neuroradiol. 2015;25:151–5.

34. Bernasconi A, Cendes F, Theodore WH, Gill RS, Koepp MJ, Hogan RE, et al. Recommendations for the use of structural magnetic resonance imaging in the care of patients with epilepsy: A consensus report from the International League Against Epilepsy Neuroimaging Task Force. Epilepsia. 2019;60:1054–68.

35. Wellmer J, Quesada CM, Rothe L, Elger CE, Bien CG, Urbach H. Proposal for a magnetic resonance imaging protocol for the detection of epileptogenic lesions at early outpatient stages. Epilepsia. 2013;54:1977–87.

36. Sternberger LA, Sternberger NH. Monoclonal antibodies distinguish phosphorylated and nonphosphorylated forms of neurofilaments in situ. Proc Natl Acad Sci USA. 1983;80:6126–30.

37. Baumann N, Pham-Dinh D. Biology of Oligodendrocyte and Myelin in the Mammalian Central Nervous System. Physiol. Rev. 2001;81:871–927.

38. Vogel US, Thompson RJ. Molecular Structure, Localization, and Possible Functions of the Myelin-Associated Enzyme 2′,3′-Cyclic Nucleotide 3′-Phosphodiesterase. J. Neurochem. 1988;50:1667–77.

39. Tomassy GS, Berger DR, Chen H-H, Kasthuri N, Hayworth KJ, Vercelli A, et al. Distinct Profiles of Myelin Distribution Along Single Axons of Pyramidal Neurons in the Neocortex. Science. 2014;344:319–24.

40. Stassart RM, Möbius W, Nave K-A, Edgar JM. The Axon-Myelin Unit in Development and Degenerative Disease. Front Neurosci. 2018;12:467.

41. Nave K-A, Werner HB. Myelination of the Nervous System: Mechanisms and Functions. Annu Rev Cell Dev Biol. 2014;30:503–33.

42. Rayatpour A, Farhangi S, Verdaguer E, Olloquequi J, Ureña J, Auladell C, et al. The Cross Talk between Underlying Mechanisms of Multiple Sclerosis and Epilepsy May Provide New Insights for More Efficient Therapies. Pharmaceuticals. 2021;14:1031.

43. Zucca I, Milesi G, Medici V, Tassi L, Didato G, Cardinale F, et al. Type II focal cortical dysplasia: Ex vivo 7 T magnetic resonance imaging abnormalities and histopathological comparisons. Ann Neurol. 2016;79:42–58.

44. Liewald D, Miller R, Logothetis N, Wagner H-J, Schüz A. Distribution of axon diameters in cortical white matter: an electron-microscopic study on three human brains and a macaque. Biol Cybern. 2014;108:541–57.

45. Tomasi S, Caminiti R, Innocenti GM. Areal Differences in Diameter and Length of Corticofugal Projections. Cereb Cortex. 2012;22:1463–72.

46. Zhou Q, Anderson DJ. The bHLH Transcription Factors OLIG2 and OLIG1 Couple Neuronal and Glial Subtype Specification. Cell. 2002;109:61–73.

47. Lu QR, Sun T, Zhu Z, Ma N, Garcia M, Stiles CD, et al. Common Developmental Requirement for Olig Function Indicates a Motor Neuron/Oligodendrocyte Connection. Cell. 2002;109:75–86.

48. Hornig J, Fröb F, Vogl MR, Hermans-Borgmeyer I, Tamm ER, Wegner M. The Transcription Factors Sox10 and Myrf Define an Essential Regulatory Network Module in Differentiating Oligodendrocytes. Barres BA, editor. PLoS Genet. 2013;9:e1003907.

49. Almeida RG, Lyons DA. On Myelinated Axon Plasticity and Neuronal Circuit Formation and Function. J Neurosci. 2017;37:10023–34.

50. Gibson EM, Purger D, Mount CW, Goldstein AK, Lin GL, Wood LS, et al. Neuronal Activity Promotes Oligodendrogenesis and Adaptive Myelination in the Mammalian Brain. Science. 2014;344:1252304.

852

Figure Legends

Figure 1

Presurgical MRI of FCD IIa and IIb patients.

Representative 3T MRI of two patients with frontal FCD IIa and FCD IIb, illustrating their differing macroscopic phenotype. Subtle cortical thickening and blurring is seen at the gray-white matter junction in FCD IIa (arrows in a, b; a: coronal, b: axial, both FLAIR). FCD IIb presents with a transmantle and deep sulcus sign (arrows in c, d; c: FLAIR, d: T2 STIR; both coronal).

Figure 2

Histological characteristics of control, FCD IIa and FCD IIb specimens.

Representative photomicrographs of cresyl violet-stained (a, d, g) and NeuN- (all neurons) (b, e, h) or SMI32-immunolabeled (pyramidal neurons in layers III and V) tissue sections (c, f, i). The FCD IIa case shows a radial lamination disturbance with hypercolumnization (d, e). In controls and FCD IIa, SMI32-positive pyramidal neurons are densely arranged in layers III and V (c, f) with the appearance of dysmorphic neurons across all layers in FCD IIa but concentrated in supragranular layers in FCD IIb (l). Detailed images of SMI32-positive cells reveal the characteristic shape of dysmorphic neurons in FCD IIa (j) and FCD IIb (k). The hallmark of FCD IIb is the presence of Balloon cells which are visualized by vimentin staining (l).

WM: white matter; Scale bars: (a-i) 250 µm; (j-l) 20 µm. I-VI: cortical layers.

Figure 3

Distribution of *mbp* mRNA-expressing OLs in control and FCD II specimens. Representative photomicrographs of cresyl violet-stained (a, d, g) and *mbp*-ISHH-processed (b, c, e, f, h, i) tissue sections of controls (a-c), FCD IIa (d-f) and FCD IIb (g-i) cases. ROIs in (b, e, h) indicate the magnified areas shown on the right. In control and FCD IIb specimens, a gradient of *mbp* mRNA-expressing cells with the highest densities in the deeper cortical layers and the white matter can be observed. This gradient is less pronounced in FCD IIa. Counting of *mbp* mRNA-expressing OLs in all cortical layers does not reveal significant differences between the groups (one-way ANOVA F=2.64, p=0.106) (j). Individual patients are color-coded: greenish: control, blueish: FCD IIa, redish: FCD IIb.

WM, white matter; scale bars: (a, b, d, e, g, h) 250 µm; (c, f, i) 100 µm, I-VI, cortical layers

Figure 4

Myelination pattern in control, FCD IIa and IIb cases from the frontal lobe. Representative photomicrographs of tissue sections immunolabeled for CNPase to identify myelinated fibers in the gray matter of control (a), FCD IIa (b) and FCD IIb (c) cases. The radially aligned CNPase-positive fibers reach the border of layer I in all cases. (d, e, f) CNPase-immunolabeled sections (red) counterstained with DAPI (blue) of control (d), FCD IIa (e) and FCD IIb (f) cases were imaged by confocal laser microscopy in layers V and VI. Individual micrographs of confocal stacks are shown. In controls, a dense network of horizontally and radially oriented CNPase-labeled fiber strands is

present. White dots (asterisks) represent pre-OL and OL cell bodies (double labeled by CNPase and DAPI) (d). This pattern of myelinated fibers is rather disorganized in FCD IIa (e) but similar to control in FCD IIb (f). (g) Quantification of CNPase-expressing pre-OL and OL cell bodies across all six layers reveals similar cell numbers in all cases (one-way ANOVA F=0.74, p=0.49). Colored dots identify individual patients, greenish: control, blueish: FCD IIa, redish: FCD IIb.

Scale bars: (a-c) 250 µm; (d-f) 20 µm; Asterisks in d, e, f: CNPase-positive pre-OL and OL cell bodies. WM, white matter. I-VI: cortical layers.

Figure 5

Ultrastructure of myelinated axons in FCD II types of the frontal lobe. Representative electron photomicrographs of myelinated axons in layers V/VI of control (a), FCD IIa (b) and FCD IIb (c) specimens. (d) Bar graph demonstrating that the mean axon diameters of FCD IIa and FCD IIb have on average larger axon diameters than control cases (one-way ANOVA F=2.59, p=0.129). (e) The cumulative frequency distribution of axon diameters shows significantly increased axon diameters in both FCD II types (one-way ANOVA F=19.26, p<0.0001; Tukey's post hoc test: control vs. FCD IIa p<0.0001, control vs. FCD IIb p<0.0001)]. (f) The mean g-ratio value is significantly increased in FCD IIa cases when compared to controls (one-way ANOVA F=4.511, p=0.044; Tukey's post hoc test: control vs. FCD IIa p=0.039). (g) The cumulative frequency distribution of g-ratios shows significant higher g-ratios for FCD IIb and FCD IIa [(one-way ANOVA F=14.69, p<0.0001; Tukey's post hoc test: control vs. FCD IIa p<0.0001, control vs. FCD IIb p=0.019, FCD

IIa vs. FCD IIb p=0.046)]. (h) Bar graph demonstrating the mean myelin sheath thickness which is similar in the three analyzed groups (one-way ANOVA F=0.746, p=0.501). (i) The cumulative frequency distribution of myelin sheath thickness does not reveal differences between controls and FCD IIa but a significant increase of FCD IIb in comparison to FCD IIa and controls [(one-way ANOVA F=4.487, p=0.012; Tukey's post hoc tests: control vs. FCD IIb p=0.023, FCD IIa vs. FCD IIb p=0.024)]. (j-l) Correlation plots of axon diameters versus myelin sheath thickness. (j) Controls, (k) FCD IIa and (l) FCD IIb. There is a significant correlation of axon diameters and the thickness of myelin sheaths for controls (Pearson's correlation: r=0.329, p=0.0003) and FCD IIb (Pearson's correlation: r=0.309, p=0.0007) but not for FCD IIa (Pearson' correlation: r=0.138, p=0.056). Colored dots represent individual patients, greenish: control, blueish: FCD IIa, redish: FCD IIb. Scale bars (a-c): 250 nm.

Figure 6

Expression levels of transcription factor and myelin-associated transcripts in frontal lobe FCD IIa and IIb.

The mRNAs levels were quantified by real-time RT-qPCR. The expression of the transcription factor mRNAs *olig2* (Kruskal-Wallis p=0.793) (a) and *sip1* (one-way ANOVA F=0.648, p=0.534) (b) are similar in all groups. The mRNA levels of *myrf* (c) and of the myelin components *mpb* (d), *mag* (e) and *mog* (f) are significantly reduced in FCD IIa when compared to FCD IIb [(*myrf*: one-way ANOVA F=7.914, p=0.003; Tukey's post hoc test: control vs. FCD IIa p=0.389, control vs. FCD IIb p=0.205, FCD IIa vs. FCD IIb p=0.002) (*mbp*:

one-way ANOVA F=5.964, p=0.009; Tukey's post hoc test: control vs. FCD IIa p= 0.672, control vs. FCD IIb p=0.190, FCD IIa vs. FCD IIb p=0.008), (*mag*: one-way ANOVA F=11.46, p=0.0005; Tukey's post hoc test: control vs. FCD IIa p=0.288, control vs. FCD IIb p=0.099, FCD IIa vs. FCD IIb p=0.0004), (*mog*: one-way ANOVA F= 7.551, p=0.004; Tukey's post hoc test: control vs. FCD IIa p=0.163, control vs. FCD IIb p=0.515, FCD IIa vs. FCD IIb p=0.003)]. Colored dots represent individual patients, greenish: control, blueish: FCD IIa, redish: FCD IIb.

Figure 7

Transcription factor binding capacities to promoters of myelin-associated genes.

OLIG2 (a-d) and MYRF (e-g) binding sites were precipitated using ChIP assays and quantified using real-time qPCR. The amounts of precipitated DNA are presented as the percentage of input DNA. The binding capacities of OLIG2 to the *SIP1* (a), *MBP* (b), *CNP* (c) and *MOG* (d) promoters are similar in all analyzed groups [(OLIG2 on *SIP1*: one-way ANOVA F=0.153, p=0.859), (OLIG2 on *MBP*: one-way ANOVA F=0.247, p=0.784), (OLIG2 on *CNP*: one-way ANOVA F=0.654, p=0.531), (OLIG2 on *MOG*: Kruskal-Wallis p=0.475)]. However, MYRF has significantly lower binding potential to the *MBP* (f), *SOX10* (g) and *MAG* (h) promoters in FCD IIa when compared to FCD IIb [(MYRF on *SOX10*: one-way ANOVA F=10.51, p=0.0008; Tukey's post hoc test: control vs. FCD IIa p=0.0009, control vs. FCD IIb p= 0.112, FCD IIa vs. FCD IIb p= 0.024), (MYRF on *MBP:* one-way ANOVA F=6.55, p=0.007; Tukey's post hoc test: control vs. FCD IIa p=0.032, control vs. FCD IIb p=

0.976, FCD IIa vs. FCD IIb p= 0.011), (MYRF on *MAG:* Kruskal-Wallis p=0.003; Dunn‘s multiple comparison test: control vs. FCD IIa p=0.017, control vs. FCD IIb p>0.999, FCD IIa vs. FCD IIb p=0.041)]. Correlation of MYRF binding capacities with *mpb* (i) and *mag* (j) mRNA expression levels. Pearson’s correlation was performed for the percentage of input values from the ChIP assays with the relative expression values of the RT-qPCRs. Significant correlations are present between MYRF binding capacities and *mpb* (i) and *mag* (j) mRNA levels, in particular for FCD IIb (Pearson’s correlation: r=0.546, p=0.009) and *mag* (Pearson’s correlation: r=0.539, p=0.009). Colored dots represent individual patients, greenish: control, blueish: FCD IIa, redish: FCD IIb.

Table 1. Clinical data of FCD IIa (A), FCD IIb (B) and controls (C) selected for this study.

A. FCD IIa cases

ID	Color code	Sex	Age at epilepsy onset (years)	Age at surgery (years)	Epilepsy duration (years)	Seizure type	Seizure frequency/ day	Neuro-pathology	MRI findings	Brodmann area	Methods applied
1		m	0.2	6	5,8	FA	n.a., during night	IIa	FCD	8	IHC, ISHH, PCR, ChIP
2		m	8	22	14	FA, FIA, BTCS	2-3	IIa	TM-FCD	10	IHC, ISHH, PCR, ChIP
3		f	2	8	6	FA	>1	IIa	FCD	8	IHC, EM, ISHH, PCR, ChIP
4		f	18	23	5	FA, FIA, BTCS	0.07	IIa	Neg.	9	IHC, EM, ISHH, PCR, ChIP
5		f	10	18	8	FA, FIA	8-10	IIa	Neg.	9	IHC, EM, ISHH, PCR, ChIP
5		f	15	18	3	FA, FIA, BTCS	0.04	IIa	FCD	n. a.	IHC, ISHH, PCR, ChIP
7		m	0.6	10	9.4	FA, FIA	4.5	IIa	FCD	9	IHC, EM, PCR, ChIP
8		f	1	8	7	FIA	0.36	IIa	FCD	9	IHC, PCR, PCR, ChIP
9		m	4	38	34	FA, FIA	3	IIa	Neg.	44	IHC, PCR, PCR, ChIP

B. FCD IIb cases

ID	Color code	Sex	Age at epilepsy onset (years)	Age at surgery (years)	Epilepsy duration (years)	Seizure type	Seizure frequency/ day	Neuro-pathology	MRI findings	Brodmann area	Methods applied
1		m	7.0	48	41.0	FA, BTCS	0.1, during night	IIb	TM-FCD	6	IHC, EM, ISHH, PCR, ChIP
2		m	5	36	31	FA, FIA	6	IIb	TM-FCD,	8	IHC, EM, ISHH, PCR, ChIP
3		f	9	45	36	FA, BTCS	0.29	IIb	TM-FCD	6	IHC, ISHH, PCR, ChIP
4		f	9	27	18	FA	1	IIb	TM-FCD	n.a.	IHC, ISHH, PCR, ChIP
5		f	12	40	28	FA, BTCS	1	IIb	TM-FCD	8	IHC, EM, ISHH, PCR, ChIP
6		m	14	23	9	FA, FIA, BTCS	1	IIb	TM-FCD	8	IHC, EM, ISHH, PCR, ChIP
7		m	9	38	29	FA, BTCS	1.2	IIb	TM-FCD	6	ISHH, PCR, ChIP
8		f	3	12	9	FA, BTCS	multiple	IIb	TM-FCD	6	IHC, PCR, PCR, ChIP
9		f	16	34	18	FIA, BTCS	0.004	IIb	TM-FCD	44, 45	IHC, PCR, ChIP

C. Control cases

ID	Color code	Sex	Age at epilepsy onset (years)	Age at surgery (years)	Epilepsy duration (years)	Seizure type	Seizure frequency/ day	MRI findings	Brodmann area	Methods applied
1		f	19	26	7	FIA, BTCS	0.43	GG	10	IHC, EM, ISHH, PCR
2		m	12	17	5	FIA, BTCS	2-3	Cystic lesion	10	IHC, EM, ISHH, PCR
3		m	2	10	8	FIA, BTCS	2	Cystic lesion	9	IHC, EM, ISHH, PCR
4		f	2	14	12	FA	1	Blurring of GM-WM boundary	11	IHC, EM, ISHH, PCR

ChIP, chromatin immunoprecipitation; BTCS: focal to bilateral tonic-clonic seizures; EM, electron microscopy; FA: focal aware seizures; FCD, focal cortical dysplasia; FIA: focal impaired awareness seizures; GG, ganglioglioma; GM, gray matter; IHC, immunohistochemistry; ISHH, *in situ* hybridization histochemistry; n.a., not available; neg., negative; PCR, polymerase chain reaction; TM, transmantle sign; WM, white matter.

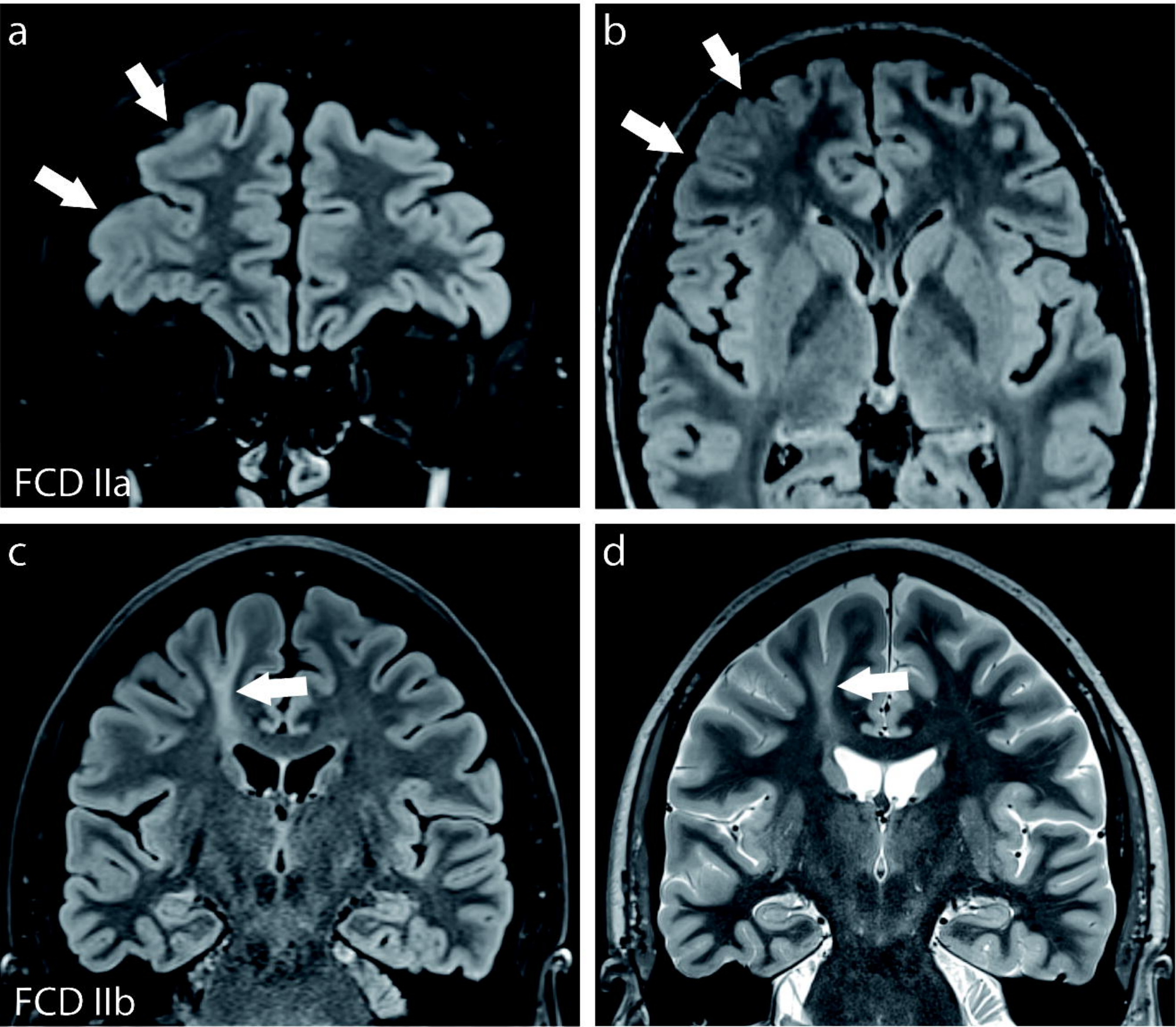
a
FCD IIa
b
c
FCD IIb
d

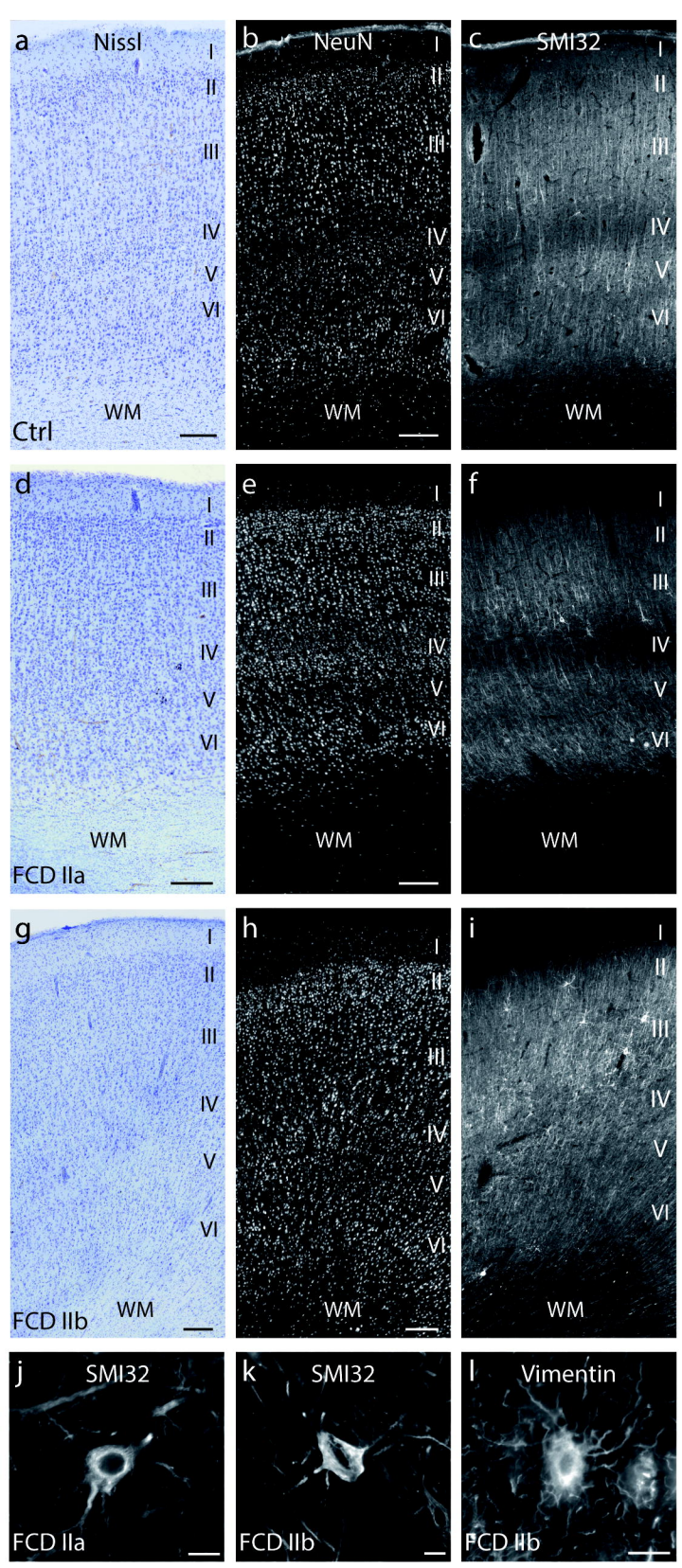
a
Nissl
I
II
III
IV
V
VI
WM
Ctrl
b
NeuN
c
SMI32
d
FCD IIa
e
f
g
FCD IIb
h
i
j
SMI32
FCD IIa
k
SMI32
FCD IIb
l
Vimentin
FCD IIb

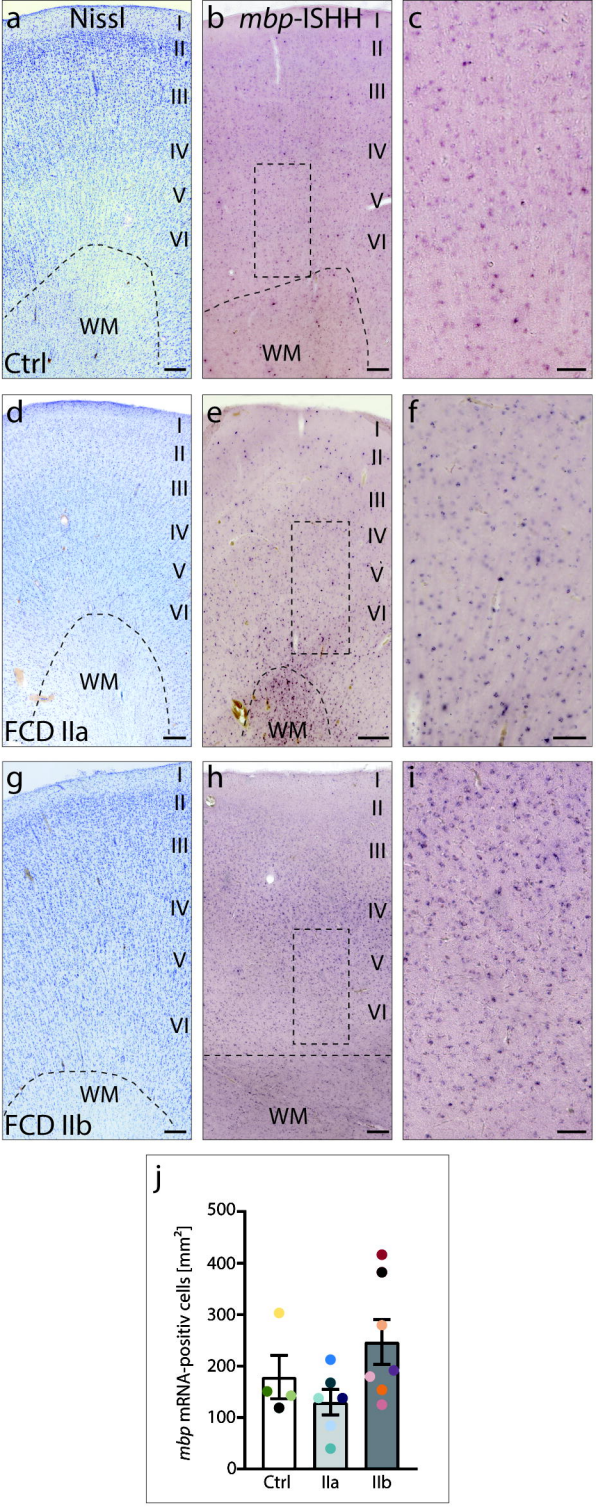
a
Nissl
b
mbp-ISHH
c
d
e
f
g
h
i
I
II
III
IV
V
VI
WM
Ctrl
FCD IIa
FCD IIb
j
mbp mRNA-positiv cells [mm²]
500
400
300
200
100
0
Ctrl
IIa
IIb

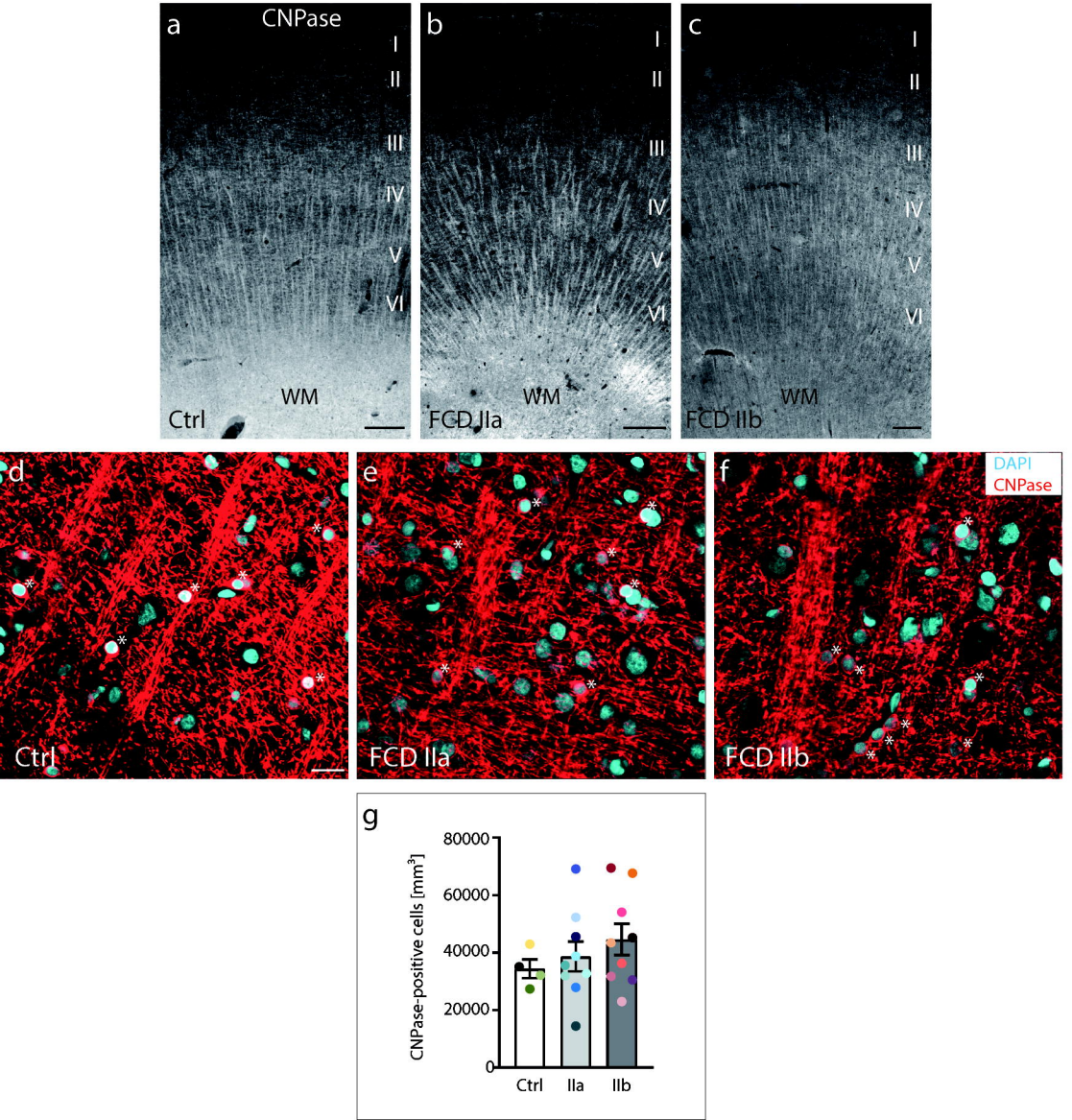
a
CNPase
I
II
III
IV
V
VI
WM
Ctrl
b
FCD IIa
c
FCD IIb
d
e
f
DAPI
CNPase
g
CNPase-positive cells [mm³]
80000
60000
40000
20000
0
Ctrl
IIa
IIb

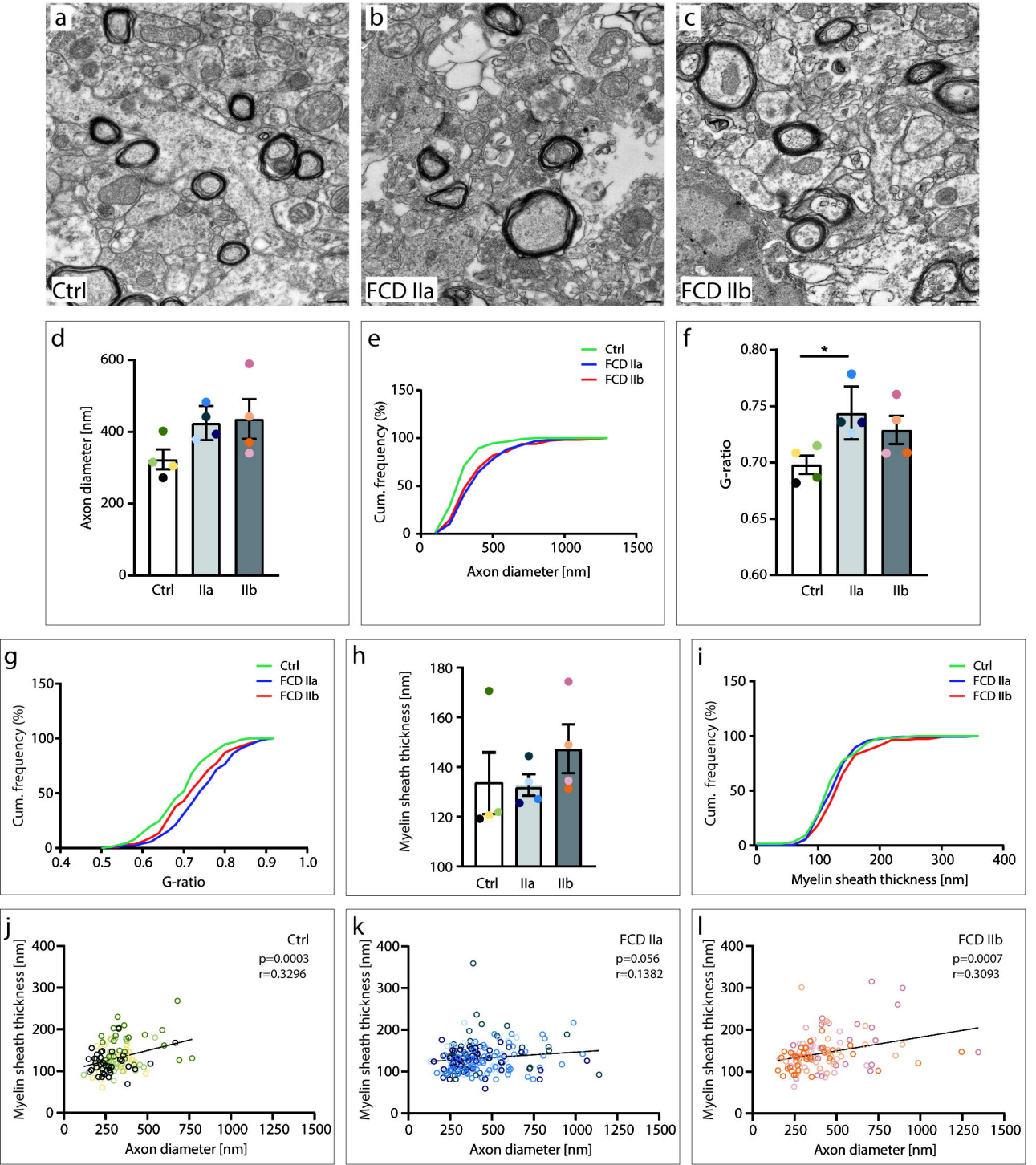
a
Ctrl
b
FCD IIa
c
FCD IIb
d
Axon diameter [nm]
600
400
200
0
Ctrl
IIa
IIb
e
Ctrl
FCD IIa
FCD IIb
Cum. frequency (%)
150
100
50
0
0
500
1000
1500
Axon diameter [nm]
f
*
G-ratio
0.80
0.75
0.70
0.65
0.60
Ctrl
IIa
IIb
g
Ctrl
FCD IIa
FCD IIb
Cum. frequency (%)
150
100
50
0
0.4
0.5
0.6
0.7
0.8
0.9
1.0
G-ratio
h
Myelin sheath thickness [nm]
180
160
140
120
100
Ctrl
IIa
IIb
i
Ctrl
FCD IIa
FCD IIb
Cum. frequency (%)
150
100
50
0
0
100
200
300
400
Myelin sheath thickness [nm]
j
Ctrl
p=0.0003
r=0.3296
Myelin sheath thickness [nm]
400
300
200
100
0
0
250
500
750
1000
1250
1500
Axon diameter [nm]
k
FCD IIa
p=0.056
r=0.1382
Myelin sheath thickness [nm]
400
300
200
100
0
0
250
500
750
1000
1250
1500
Axon diameter [nm]
l
FCD IIb
p=0.0007
r=0.3093
Myelin sheath thickness [nm]
400
300
200
100
0
0
250
500
750
1000
1250
1500
Axon diameter [nm]

Transcription Factors

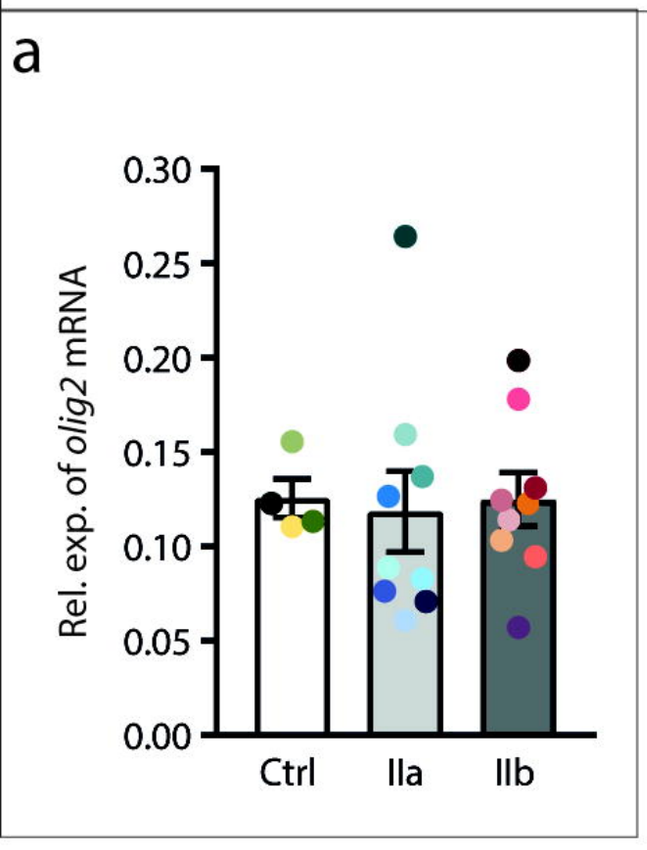

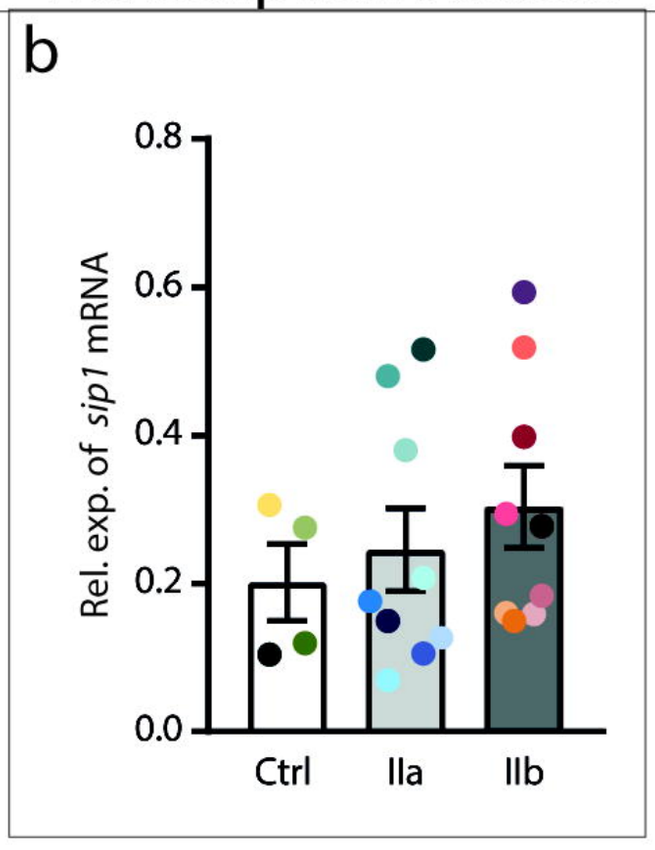

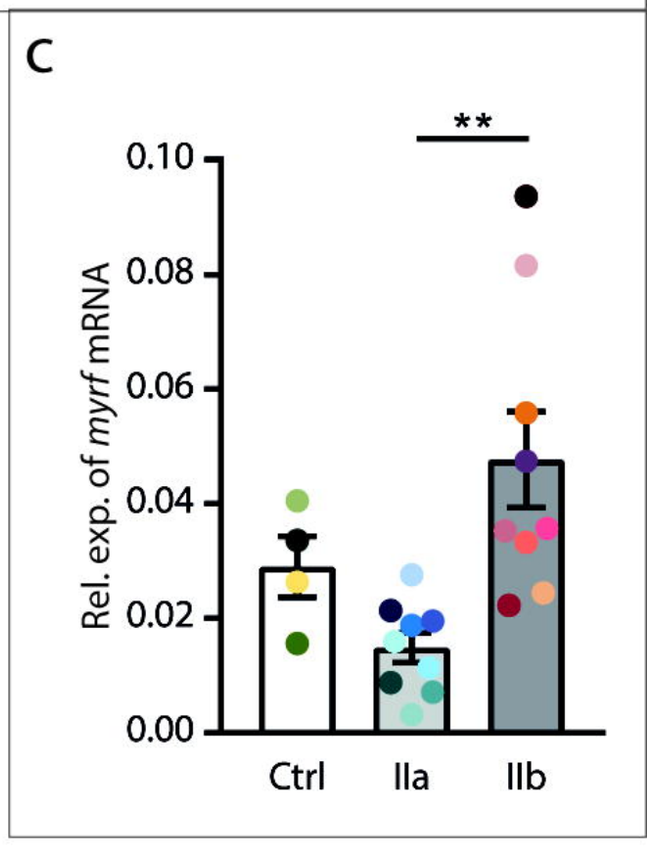

Structural Myelin Proteins

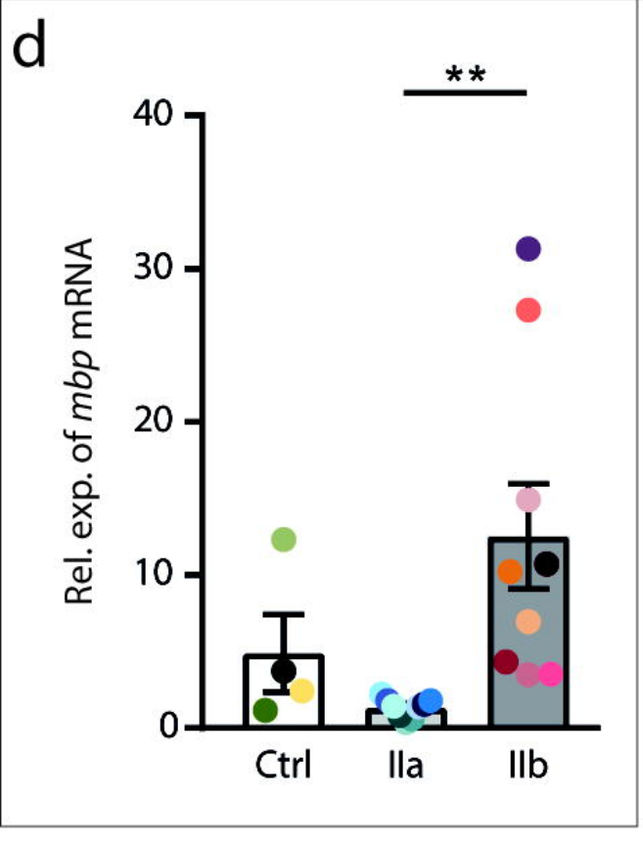

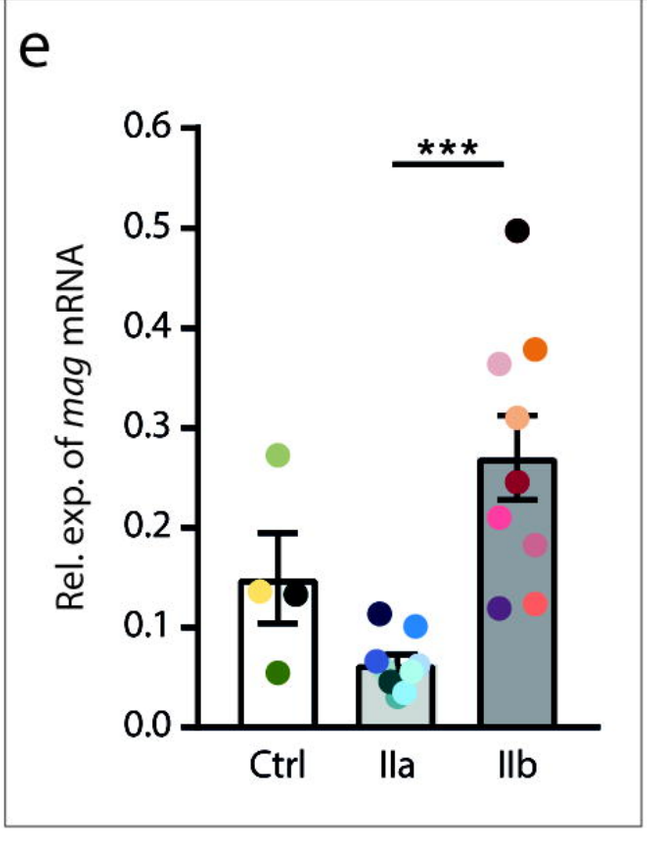

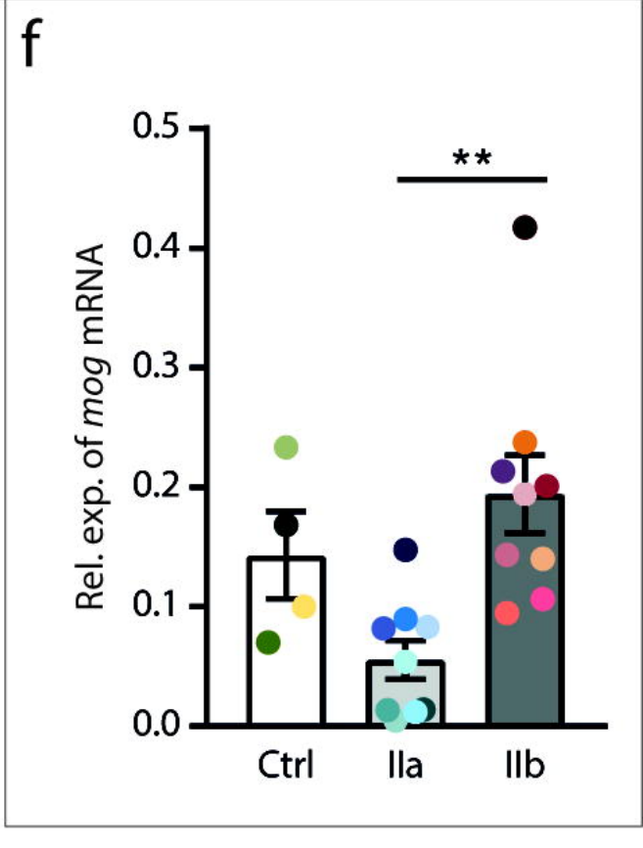

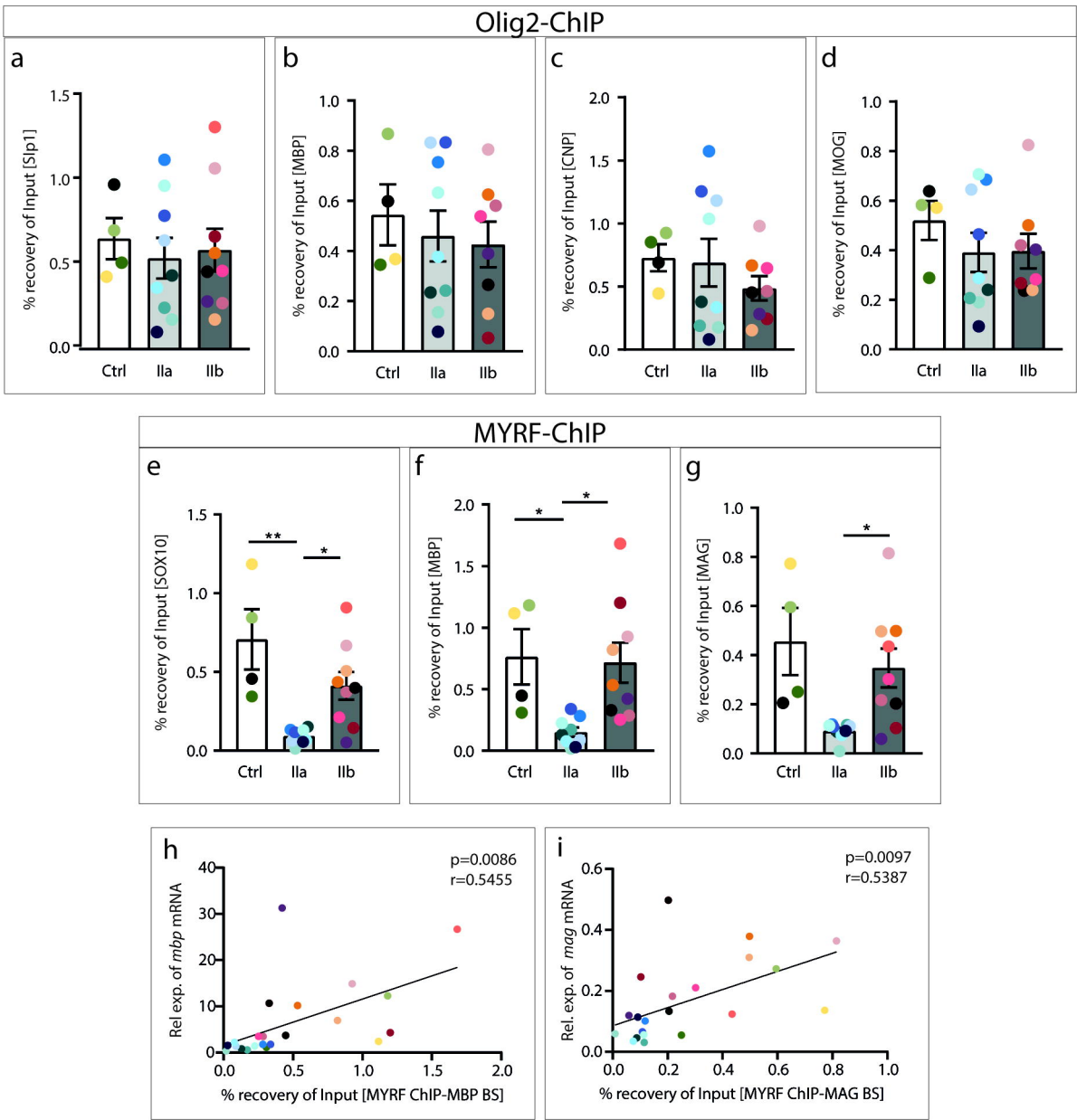
Olig2-ChIP
a
% recovery of Input [Slp1]
1.5
1.0
0.5
0.0
Ctrl
IIa
IIb
b
% recovery of Input [MBP]
1.0
0.8
0.6
0.4
0.2
0.0
Ctrl
IIa
IIb
c
% recovery of Input [CNP]
2.0
1.5
1.0
0.5
0.0
Ctrl
IIa
IIb
d
% recovery of Input [MOG]
1.0
0.8
0.6
0.4
0.2
0.0
Ctrl
IIa
IIb
MYRF-ChIP
e
% recovery of Input [SOX10]
1.5
1.0
0.5
0.0
**
*
Ctrl
IIa
IIb
f
% recovery of Input [MBP]
2.0
1.5
1.0
0.5
0.0
*
*
Ctrl
IIa
IIb
g
% recovery of Input [MAG]
1.0
0.8
0.6
0.4
0.2
0.0
*
Ctrl
IIa
IIb
h
p=0.0086
r=0.5455
Rel exp. of mbp mRNA
40
30
20
10
0
0.0
0.5
1.0
1.5
2.0
% recovery of Input [MYRF ChIP-MBP BS]
i
p=0.0097
r=0.5387
Rel. exp. of mag mRNA
0.6
0.4
0.2
0.0
0.0
0.2
0.4
0.6
0.8
1.0
% recovery of Input [MYRF ChIP-MAG BS]